Chapter 6

Natural Convection in a Large Channel with Asymmetric Radiative Coupled Isothermal Plates

Abstract. Finite volume numerical computations have been carried out in order to obtain a correlation for the heat transfer in large air channels made up by an isothermal plate and an adiabatic plate, considering radiative heat transfer between the plates and different inclination angles. Numerical results presented are verified by means of a post-processing tool to estimate their uncertainty due to discretization. A final validation process has been done by comparing the numerical data to experimental fluid flow and heat transfer data obtained from an ad-hoc experimental set-up.

6.1   Introduction

An important effort has already been done by many authors towards to study the natural convection between parallel plates for electronic equipment ventilation purposes. In such situations, since channels are short and the driving temperatures are not high, the flow is usually laminar, and the physical phenomena involved can be studied in detail both by means of experimental and numerical techniques. Therefore, a large experience and much information is available [1][2][3]. In fact, in vertical channels with isothermal or isoflux walls and for laminar flow, the fluid flow and heat transfer can be described by simple equations arisen from the analytical solutions of the natural convection boundary layer in isolated vertical plates and the fully developed flow between two vertical plates.

Ventilation channels with larger dimensions are frequently encountered in other applications such as solar energy (ventilated facades). These channels involve more complex physical phenomena as radiative heat transfer between the walls of the channel, turbulent flow, and inclination respect to the gravity direction. Although the equations developed for simpler situations in some cases could lead to reasonable predictions of the behavior of these channels, work is still required so as to have more reliable expressions.

The work here presented is addressed to obtain equations for the heat transfer in large air channels with asymmetric radiative coupled isothermal plates and considering different inclinations. Correlations of the Nusselt number are obtained from a parametric study carried out by means of high level Computational Fluid Dynamics (CFD) calculations based on finite-volume techniques. The numerical solutions are verified using a post-processing tool based on the Richardson extrapolation theory and on the Grid Convergence Index (GCI) that estimates their uncertainty due to discretization [4][5]. Furthermore, in order to know how far the numerical model is from the reality, results of the numerical model are validated by comparison to experimental fluid flow and heat transfer data obtained from an ad-hoc experimental set-up.

6.2   Description of the studied problem

A schematic of the problem under study is shown in Fig. 6.1a. It consists of a large air channel ($Pr = 0.71$) that can be positioned vertically or inclined, with an isothermal wall and an adiabatic wall (respectively upper and lower walls when the channel is inclined). The channel length L varies from $L = 1\ m$ to $L = 2\ m$ and the inter-plate spacing b can vary from $b = 0.01\ m$ to $b = 0.04\ m$ leading to aspect ratios from $L/b = 25$ to $L/b = 200$. The inclination of the channel is referenced by the angle θ and varies from $\theta = 0^o$ (vertical channel) to $\theta = 60^o$. Radiative heat transfer
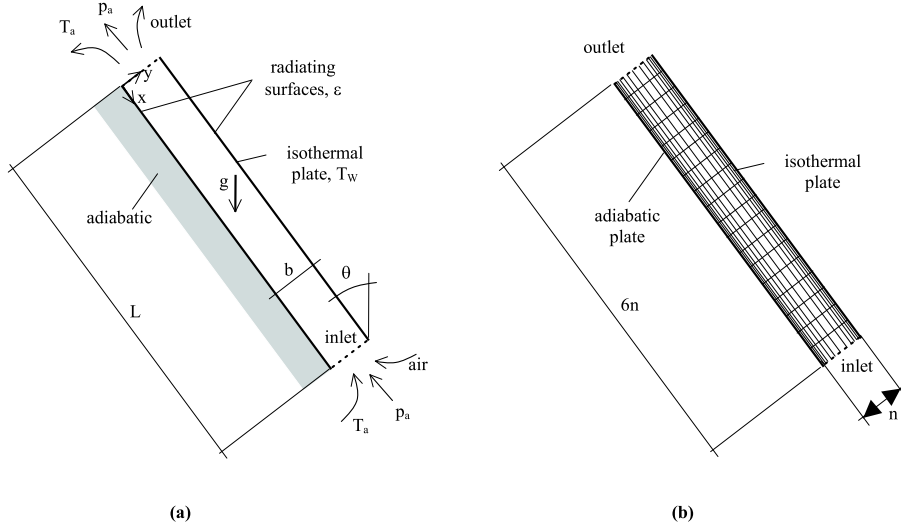
Figure 6.1: (a) Schematic of the studied problem. (b) Mesh and computational domain used in the numerical simulations. The mesh is expressed in terms of the parameter n. The solid triangles indicate that the mesh has been concentrated near the walls.

between the two walls is considered. Both plates have the same emissivity ϵ that can have a value from $\epsilon = 0$ corresponding to non-radiating surfaces (white surfaces) to $\epsilon = 1$ (black surfaces). The isothermal plate temperature, T_w, reaches values from $T_w = T_a + 25^oC$ to $T_w = T_a + 125^oC$, where T_a is the ambient temperature.

In the limiting case with non radiating plates ($\epsilon = 0$), heat transfer is only due to convection at the isothermal plate. In other cases, heat transfer to the air is also due to the heat radiation from the isothermal plate to the adiabatic plate which, in his turn, transfers the radiating energy to the surrounding air by convection.

The global Nusselt number accounting for the natural convection in channels with isothermal walls is typically defined in terms of the inter-plate spacing b as follows

$$Nu_b = \left[\frac{Q/A}{(T_w - T_a)} \right] \frac{b}{\lambda} \tag{6.1}$$

where λ is the air thermal conductivity, Q is the total rate of heat transfer from the plates to the air and A is the surface of the heat source. In the case under study A represents the surface of the isothermal plate.

Transition from laminar to turbulent flow in natural convection vertical boundary layers is typically assumed at $Gr_L = Ra_L/Pr = [g\beta(T_w - T_a)L^3/\nu^2] = 10^9$, where Gr is the Grashof number, the subindex L means that the channel length is used as geometrical parameter, g is the gravitational acceleration, and β and ν are the volumetric coefficient of thermal expansion and the kinematic viscosity of the air at the film temperature $(T_w + T_a)/2$. Transition from laminar to turbulent flow in channels, though, is expected to occur at higher values of Gr_L due to the merging effect of the two boundary layers. Most situations under study in this work have a Gr_L number in the order of 10^{10}. Therefore the assumption of laminar flow may apply. In fact, some numerical experiments not presented here have been carried out using two equations turbulent models as those used in [6] . The results showed that these turbulent models did not predict turbulence within the channel.

6.3   Mathematical model

6.3.1   Governing equations

The fluid flow and heat transfer within the channel is assumed to be governed by the two-dimensional Navier-Stokes equations together with the energy equation with the following restrictions: steady state, laminar flow, constant physical properties, density variations are relevant only in the buoyancy terms of the momentum equations (Boussinesq approximation), fluid Newtonian behavior, negligible heat friction and influence of pressure on temperature, non-participant radiating medium. The corresponding set of differential equations may be written:

$$\frac{\partial u}{\partial x} + \frac{\partial v}{\partial y} = 0 \tag{6.2}$$

$$\rho u \frac{\partial u}{\partial x} + \rho v \frac{\partial u}{\partial y} = -\frac{\partial p_d}{\partial x} + \mu \left(\frac{\partial^2 u}{\partial^2 x} + \frac{\partial^2 u}{\partial^2 y} \right) - \rho\beta(T - T_o)g_x \tag{6.3}$$

$$\rho u \frac{\partial v}{\partial x} + \rho v \frac{\partial v}{\partial y} = -\frac{\partial p_d}{\partial y} + \mu \left(\frac{\partial^2 v}{\partial^2 x} + \frac{\partial^2 v}{\partial^2 y} \right) - \rho\beta(T - T_o)g_y \tag{6.4}$$

$$\rho u \frac{\partial T}{\partial x} + \rho v \frac{\partial T}{\partial y} = \frac{\lambda}{c_p} \left(\frac{\partial^2 T}{\partial^2 x} + \frac{\partial^2 T}{\partial^2 y} \right) \tag{6.5}$$

where (x, y) are the coordinates in the Cartesian-coordinate system x-y indicated in Fig. 6.1a; T is the temperature; T_o the reference temperature; p_d the dynamic

pressure; (u, v) and (g_x, g_y) the velocity and the gravitational acceleration vector expressed in the reference system x-y, and the physical properties of the air $\rho, \mu, \beta, \lambda$ and c_p are respectively: the density, the dynamic viscosity, the thermal expansion coefficient, the thermal conductivity and the specific heat at constant pressure, which are assumed constant ($Pr = 0.71$).

6.3.2 Boundary conditions

The temperature of the isothermal plate (upper plate) is T_w. On the other hand, the temperature at the coordinate x of the adiabatic plate, results from a surface heat balance considering that the net radiative heat incoming the plate equals the heat transfered from the plate to the surrounding air:

$$\frac{\epsilon}{2 - \epsilon}\sigma(T_w^4 - T^4)\bigg|_{(x,y=0)} = -\lambda\frac{\partial T}{\partial y}\bigg|_{(x,y=0)} \tag{6.6}$$

where σ is the Stefan-Boltzmann constant and λ is the thermal conductivity of the air. In this heat balance, the radiative heat transfer between the plates (left term of the equality) is modeled assuming non-participating media, infinite surfaces, and grey-diffuse plate surfaces with the identic emissivity value ϵ.

The boundary conditions to be assumed at the inlet and outlet are rather more complicated because an inappropriate formulation of these boundary conditions may lead to a fluid flow and heat transfer very different from that under study. Typical assumptions adopted for free convective flow through channels are here adopted, see [2]. The air is assumed to enter at the channel from the surroundings with a temperature equal to T_a (ambient temperature) and with an adiabatic and reversible process, so that dynamic pressure energy at the surrounding air (which is 0) is converted to kinematic energy (i.e. to $\frac{1}{2}\rho\mathbf{v}^2$, where $\mathbf{v}$ is the module of the velocity vector) and dynamic pressure energy at the inlet:

$$T|_{(x=L,y)} = T_a \qquad 0 = \frac{1}{2}\rho\mathbf{v}^2 + p_d\bigg|_{(x=L,y)} \tag{6.7}$$

At the outlet the temperature is assumed to remain constant in the x direction and all the kinematic energy of the air is assumed to be converted to heat, resulting into an outlet dynamic pressure equal to the surrounding air dynamic pressure, i.e. equal to 0:

$$\frac{\partial T}{\partial x}\bigg|_{(x=0,y)} = 0 \qquad p_d|_{(x=0,y)} = 0 \tag{6.8}$$

6.3.3   Governing numbers

A non-dimensionalisation of the governing equations and of the boundary conditions shows that Nu_b depends on the Rayleigh number, the aspect ratio, the inclination, the plates thermal emissivity and on two radiation numbers, Pl and R, that arise from the adiabatic wall boundary condition when radiative heat transfer is considered. Thus:

$$Nu_b = Nu_b(Ra_b, b/L, cos\theta, \epsilon, P_l, R) \qquad (6.9)$$

where the Rayleigh number in terms of the geometrical parameter b is defined as $Ra_b = [g\beta(T_w - T_a)b^3/\nu^2]Pr$. The radiation numbers are the Planck number $Pl = \lambda/b\sigma T_a^3$ and $R = (T_w - T_a)/T_a$, where σ is the Stefan-Boltzmann constant and λ is the air thermal conductivity at the film temperature.

6.4   Numerical model

The set of coupled partial differential equations and the boundary conditions described in section 6.3 are converted to algebraic equations by means of finite-volume techniques using rectangular meshes on a staggered arrangement. Diffusive terms at the boundaries of the control volumes are evaluated by means of second order central differences, while the convective terms are approximated by means of the high order SMART scheme [7], which theoretical order of accuracy is between 1 and 3. A special treatment of the inlet and outlet pressure boundary conditions has been implemented according to [8].

The domain where the computations are performed and a schematic of the mesh adopted is shown in Fig. 6.1b. The mesh is represented by the parameter n. According to Fig. 6.1b, $6n*n$ control volumes are used (for example, when $n = 40$ it means that the problem is solved on $240*40$ control volumes). The mesh is intensified near the two plates using a tanh-like function with a concentration factor of 1, see [6], so as to properly solve the boundary layer. This aspect is indicated in the figure with two solid triangles.

The resulting algebraic equation system has been solved using a pressure based SIMPLE-like algorithm [9][10], and the iterative convergence procedure has been truncated once relative increments of the computed Nusselt (equation 6.1) in the last 50 iterations were below 0.005 per cent.

6.4.1   Verification of the numerical model

Numerical solutions here presented have been calculated adopting a h-refinement criteria. That is, all the numerical parameters are fixed (numerical scheme, numerical

case	b	L	θ	$T_w - T_a$	ϵ	$(b/L)Ra_b cos\theta$
	[m]	[m]	[deg]	[^oC]	[$-$]	[$-$]
a	0.01	1.00	30	25	0.25	$2.0 \cdot 10^1$
b	0.02	1.50	15	50	0.25	$4.8 \cdot 10^2$
c	0.03	1.75	45	75	0.50	$2.3 \cdot 10^3$
d	0.04	2.00	0	125	1.00	$1.5 \cdot 10^4$

Table 6.1: Parameters of the cases used for detailed verification purposes: inter-plate spacing (b), channel length (L), inclination angle (θ), isothermal wall temperature (T_w), ambient temperature ($T_a = 300\ K$) and plates emissivity (ϵ).

boundary conditions, etc.) and the mesh is refined obtaining a set of numerical solutions each one represented by the mesh parameter n. This set of numerical solutions have been post-processed by means of a tool based on the Richardson extrapolation theory and on the concept of Grid Convergence Index (GCI) [4][5]. When the numerical solutions are free of bugs, convergence errors and round-off errors, the computational error is only due to the discretization. The tool processes a set of three consecutive solutions in the h-refinement. The main output is an estimate of the uncertainty of the numerical solutions due to discretization, the GCI. Other information also obtained from the tool, is the order of accuracy of the numerical solution (apparent or observed order of accuracy) and the percentage of nodes with monotone convergence with the mesh (Richardson nodes, see [4]). An observed order of accuracy approaching the theoretical value (order of accuracy of the numerical schemes used) and a high percentage of Richardson nodes, indicate that the estimator GCI is reliable, and that the solution is free of bugs, convergence errors and round-off errors.

So as to show the appropriateness of the numerical parameters adopted in all the numerical solutions of this work, the results of a detailed verification process will be here discussed. The numerical parameters to be considered are the grid, the numerical scheme and the convergence criteria.

In order to obtain the final correlation for the Nusselt number, a parametric study of the air channel has been carried out involving up to 2500 different computations, see section. 6.6.1. Data obtained from the post-processing that are presented here, correspond to four of these computations that are representative of all the others. They will be hereafter called as case a, case b, case c and case d. Their corresponding parameters (inter-plate spacing b, channel length L, inclination angle θ, difference between isothermal wall temperature and the ambient temperature $T_w - T_a$ and plates emissivity ϵ), are presented in Table 6.1.

For each of the four cases, a set of 5 solutions on the h-refinement criteria with a refinement ratio of 2 (doubling the mesh) have been computed. They correspond

	case a							
	u			v			T		
grid	Rn	p	GCI^*	Rn	p	GCI^*	Rn	p	GCI^*
n	[%]		[%]	[%]		[%]	[%]		[%]
20	89	1.1	.273	87	2.0	.0017	99	1.7	.208
40	97	2.5	.013	91	2.0	.0023	84	3.9	.005
80	96	1.1	.014	89	1.8	.0010	83	1.6	.0120

	case b							
	u			v			T		
grid	Rn	p	GCI^*	Rn	p	GCI^*	Rn	p	GCI^*
n	[%]		[%]	[%]		[%]	[%]		[%]
20	75	1.9	.162	71	2.2	.0013	67	2.2	.070
40	82	0.9	.162	71	1.2	.0036	72	1.2	.068
80	91	1.9	.014	79	1.6	.0015	81	1.8	.010

	case c							
	u			v			T		
grid	Rn	p	GCI^*	Rn	p	GCI^*	Rn	p	GCI^*
n	[%]		[%]	[%]		[%]	[%]		[%]
20	78	1.3	.568	43	2.1	.0069	77	1.5	.320
40	84	2.1	.063	43	1.9	.0030	58	2.6	.020
80	88	2.0	.014	76	1.9	.0023	74	2.0	.012

	case d							
	u			v			T		
grid	Rn	p	GCI^*	Rn	p	GCI^*	Rn	p	GCI^*
n	[%]		[%]	[%]		[%]	[%]		[%]
20	63	1.6	.350	43	1.4	.0213	73	0.9	1.44
40	51	2.1	.087	48	1.6	.0080	59	2.6	.026
80	67	1.2	.087	50	1.3	.0070	59	1.2	.072

Table 6.2: Results from the post-processing tool: Richardson nodes (Rn), global observed order of accuracy (p), and global uncertainty due to discretization normalized by the reference values (GCI^*). (Note: * means that the GCIs have been normalized using a reference value of $v_{ref} = [Lg\beta(T_w - T_a)cos\theta]^{1/2}$ for the velocity components and $T_{ref} = T_w - T_a$ for the temperature).
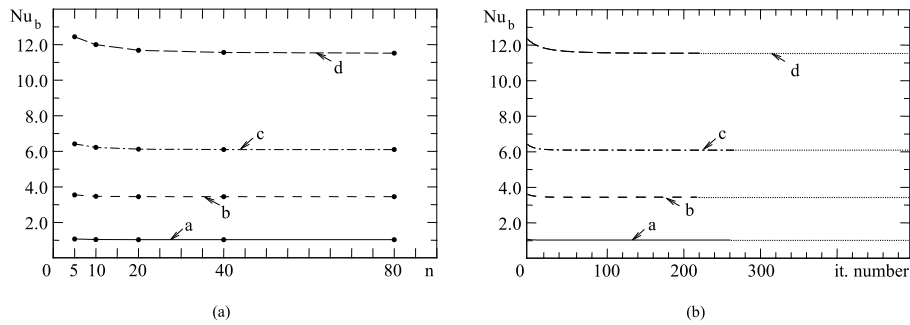
Figure 6.2: Verification. (a) Evolution of the Nu_b in terms of the mesh parameter n. (b) Evolution of the Nu_b during the convergence procedure in terms of the number of iterations. A spot line indicates that the convergence criteria has already been overcome.

to $n = 5$, 10, 20, 40 and 80. The post-processing results are given in Table 6.2 for $n = 20$, 40 and 80. Presented are the global observed order of accuracy, p, the percentage of Richardson nodes, Rn, and the global uncertainty due to discretization, GCI, corresponding to the different dependent variables of the problem u, v and T.

The percentage of Richardson nodes given in the Table is high for the cases a and b, but decreases in the cases c and d were the physical phenomena is more complex. While the two first cases have a value of the $(b/L)Ra_b cos\theta$ below $5 \cdot 10^2$, the corresponding values to the cases c and d are beyond $2 \cdot 10^3$. On the other hand, most estimates of the order of accuracy, p, approach the theoretical values of the differential scheme used (between 1 and 3). However, they do not tend to an asymptotic value with the mesh. As the GCI is directly calculated from p, GCI increases with the mesh in some situations where p degenerates with the mesh to values close to 1. This means that for those cases the calculated uncertainty due to discretization increases when the mesh is refined! This aspect is in accordance with the practice of the use of the GCI, which indicates that low values of the observed order of accuracy tend to overestimate the uncertainty due to discretization. When dealing with a single case, it may be possible to overcome this problem by just changing the numerical schemes or the discretization of the domain. Though, as in this work up to 2500 different cases are studied, it is not practical to find a particular mesh for each of them.

All the numerical solutions used in the previous discussion have been obtained using the convergence criteria as explained in the beginning of this section 6.4. This convergence criteria results in a reasonable number of iterations of the convergence procedure and, therefore, in a reasonable cpu time. However, it apparently is a non-restrictive convergence criteria. Several computations have been carried out con-

sidering various situations, including the four cases analyzed in this section, with a more restrictive convergence criteria. Some small differences have been found in the estimates obtained from the post-processing. This indicates that the numerical error of the solutions with the non-restrictive convergence criteria are not totally free of convergence error. However, the general tendency is that whenever the estimates obtained from the verification process indicated that the solution was credible, there were no variations in the value of Nu_b when the convergence criteria was strengthen.

Some of this information is given in Fig. 6.2. The evolution of the Nu_b with the mesh parameter n for the four cases is shown in Fig. 6.2a. Beyond the fourth level of refinement $n = 40$ no relevant differences are observed in the Nu_b. The evolution of the Nu_b during the iterative process in terms of the number of iterations is shown in Fig. 6.2b. A continuous line is used which turns into a spot line when the non-restrictive convergence criteria is reached. As observed, all the spot lines are horizontal lines, indicating that there are no deviations in the Nu_b when the non-restrictive convergence criteria has been reached.

6.5 Experimental set-up

The experimental set-up consists of a 45° lifted channel built-up by two parallel plates 1600 mm length and 800 mm width with a spacing of 20 mm. A schematic of the set-up is shown in Fig. 6.3. The channel is closed at its sides by two lids covered by rock wool on the external side. Two additional adiabatic lids can be mounted at the inlet and the outlet when required so as to stop the air circulation through the channel. The lower plate is a single plate insulated from the ambient by rock wool. The upper plate is made up by eight square modules of $400 * 400$ mm^2. Each module is heated by electrical heaters glued at the upper side. A self-calibrated K-type thermocouple sensor is placed at its center. Heaters of the two modules placed at the same height are connected to an AC controlled power supply, forming four pairs of modules connected to four different power lines. Four glass windows with an observation area of $20 * 20$ mm^2 are mounted at one side wall at 200, 600, 1000 and 1400 mm from the outlet of the channel in order to to permit the visualization of the air flow in the channel. The ambient temperature T_a (laboratory temperature) is measured by a self-calibrated Resistance Thermal Device PT-100. Control, regulation and data acquisition is carried out by a HP acquisition data unit series VXI managed by a software programmed in HPVEE language.

Measurements of the heat transfer and the velocity field have been performed in separate experimental campaigns. In the measurements of the heat transfer, the overall heat loss of the set-up P is measured at some specific isothermal plate temperatures, T_w, and ambient temperatures, T_a.

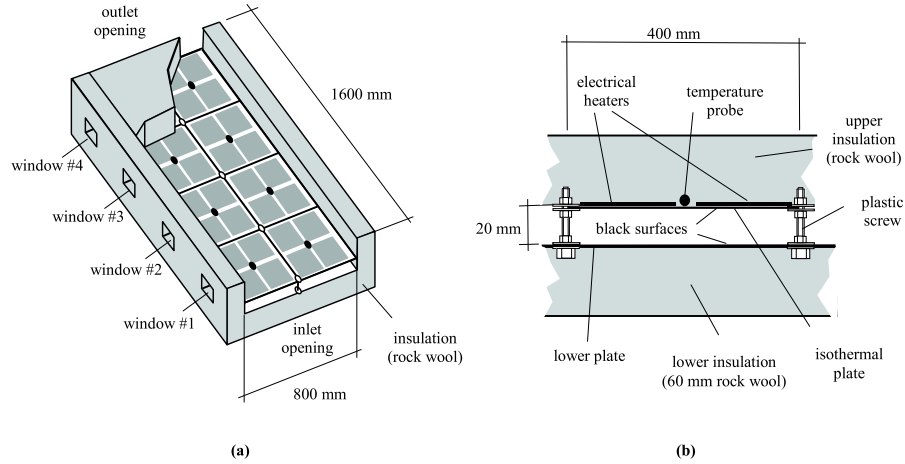In the fluid flow experiments the velocity field is visualized at a section of the

Figure 6.3: Schematic of the set up. (a) General view. (b) Detail of the modules that make up the isothermal plate.

channel parallel to and 200 *mm* from the side wall with windows at different values of $T_w - T_a$. To do so, the air is seeded by aerosols of olive oil generated by a so-called Laskin nozzle. The diameter of the aerosols are in the order of 5 *μm*. The images of the flow are captured using a Digital Particle Image Velocimetry (DPIV) facility from LaVision. Main features of the DPIV device used in the fluid flow experiments are: double-cavity Nd-YAG (2x35 mJ/pulse) laser from Quantel, optics consisting on one spherical and two cylindrical lenses forming a Galilei telescope to create and focus a light-sheet, a high sensitive (peltier-element cooled) 12 bit CCD camera with resolution of $1280 * 1024$ pixels and a Nikkor camera lens with focal length of 105 *mm*.

Details on the experimental procedures adopted for both the heat transfer and fluid flow measurements are explained in the following two subsections.

6.5.1 Measurement of the heat transfer

With both the channel open and closed, the global heat loss of the set-up, *P*, has been measured at different temperatures of the isothermal plate: T_w=70, 100, 125 and 150 ^oC. The global heat loss has been obtained by measuring the power that has been supplied to the electrical heaters. This has been realized by means of power transducers with a precision of $\pm[0.5 + 0.02P]$ *W*. Data have been recorded for a period of 15 minutes in intervals of 3 seconds when the steady state of the set-up was

reached.

Measurements of the heat loss with the channel closed have been fitted by a least squares method to a second order equation in terms of the temperature difference $\Delta T = (T_w - T_a)$. This leaded to a correlation for the experimental set-up heat loss without heat evacuation through the channel, $Q_{loss} = (a + b\Delta T)\Delta T$.

Experimental values of the heat evacuated from the channel, Q, have been calculated by subtracting the corresponding Q_{loss} from the overall measured heat loss P obtained from the experiments with the channel open. The Nusselt number has been calculated from Q according to equation (6.1).

6.5.2 Measurement of the fluid flow

Measurements of the velocity field at each window of the channel have been obtained at two different temperatures of the isothermal plate: $T_w = 70^oC$ and $T_w = 150^oC$. Each measurement consists of five series of ten data sets of velocity fields taken at a sample rate of 8 Hz, making up a total series of 50 data sets of velocity fields. From the image analyses it turned out that the maximum particle image displacements were in the order of 9 pixels. Adaptive interrogation areas from $64*64$ to $32*32$ pixels with a 50% of overlapping have been applied. Effects of in-plane loss of particle pairs have been minimized by a zero-offsetting of the interrogation areas. Errors of the measured velocities due to the DPIV device, the data acquisition and the post-processing are expected to be below $\pm 0.03\ m/s$.

Even if an optimum PIV experiment has been carried out, there is always a probability of erroneous velocity vectors, usually called outliers. Therefore, a post-processing of the PIV results is always necessary in order to detect and eliminate as many erroneous vectors as possible [11]. Outliers have been detected by the median test performed by a self-written algorithm and substituted by the local mean value of the nine surrounding velocities.

6.6 Results and discussion

6.6.1 Parametric study

A parametric study has been carried out varying the channel length L, the inter-plate spacing b, the inclination angle θ, the plates thermal emissivity ϵ and the isothermal wall temperature T_w and setting the ambient temperature at $T_a = 300\ K$. Values for each parameters have been fixed within the interval range under study and for equal sized intervals (see section 6.2). Four different values for b and five different values for the other parameters have been used. This resulted into a total number of 2500 situations. Numerical results obtained for all the situations have been calculated with

the level of refinement $n = 40$, and by using the convergence criteria and numerical schemes as explained in section 6.4. These numerical parameters are in accordance to the conclusions of the verification process as discussed in section 6.4. Conclusions of this verification process were focussed on the analysis of 4 of the 2500 situations under study. Therefore, there is no guarantee that these numerical parameters may lead to solutions free of computational errors for all the situations. Thus, so as to discard all those non-credible numerical solutions, all of them have been submitted to a verification test. It consisted in two steps. In the first step, the global observed order of accuracy p, the normalized global grid convergence index GCI^* and the percentage of Richardson nodes Rn have been calculated by means of of the post-processing tool, see 6.4. In the second step, the solutions have been filtered according to the post-processing results. The values of acceptance adopted are: p within the interval $[1 : 4]$, GCI^* below 1% and Rn over 40%. These filtering criteria has been accomplished by 1842 cases from the 2500. Values of the parameters L, b, θ, ϵ and $T_w - T_a$ of those cases that have not accomplished the criteria were rather random without clear tendencies. More restrictive filtering leaded to discard those solutions with higher values of the number $(b/L)Ra_b cos\theta$. This was mainly because the convergence with the mesh was more difficult and, as a consequence, the number of Richardson nodes was lower. Differences between the fit of the solutions that passed a more restrictive filtering and the fit of the solutions finally accepted were not relevant. Therefore, the given correlation is not expected to be disturbed by wrong-converged solutions.

6.6.2 Heat transfer relation

From the non-dimensionalisation of the governing equations and boundary conditions as discussed in section 6.3.3, it turns out that Nu_b depends on 6 different governing numbers: Ra_b, b/L, $cos\theta$, ϵ, P_l and R. By using a single group $(b/L)Ra_b cos\theta$ as correlating group instead of the three separate groups groups (b/L), Ra_b and $cos\theta$, the number of correlating numbers is reduced to 4. This is a widely adopted practice for inclined plates [3]. Furthermore, and after a first evaluation of the data to be fitted, the influence of the radiating groups (Planck number and R) was shown to be negligible. Therefore, the set of correlating number has been reduced to 2. Accordingly, data of all the 1842 solutions accomplishing the verification-filtering criteria as described in section 6.6.1 have been fitted to a heat transfer relation for the Nusselt number Nu_b in terms of the groups $(b/L)Ra_b cos\theta$ and ϵ. The resulting relation reads:

$$Nu_b = \left[\left(\frac{1}{12}(b/L)Ra_b cos\theta \right)^{-2} + \left(0.59[(b/L)Ra_b cos\theta]^{1/4}[1 + \epsilon^{4/5}]^{4/5} \right)^{-2} \right]^{-1/2} \quad (6.10)$$

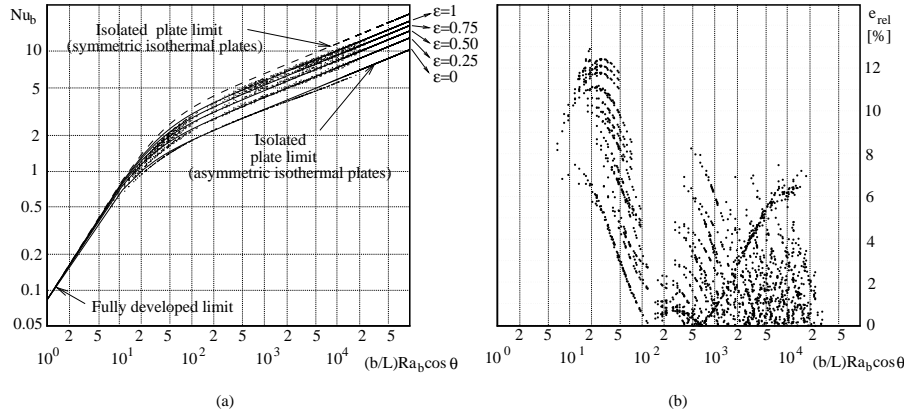The fitting process has been carried out minimizing the average of the relative dif-

Figure 6.4: Results from the fitting process. (a) Nu_b in terms of $(b/L)Ra_b cos\theta$ and ϵ. Solid lines: heat transfer relation 6.10 for different values of plates emissivity ϵ. Dashed line: relation of Bar-Cohen [1] for symmetric isothermal vertical plates using the Nu_b number as defined in equation 6.1. Dots: fitted data. (b) Relative errors between the fitted data and the heat transfer relation 6.10 in terms of $(b/L)Ra_b cos\theta$

ferences between the data and the fitting relation by means of the Powell method. Several fitting procedures have been done by fitting a different number of constants. The final fitting process actually accepted has been done by fixing all the parameters in equation (6.10), except the two exponents that affect only ϵ. Relation (6.10) has been shown to properly accommodate all the data. The maximum relative error between the fitted data and the correlation was found below 13% and the average relative error below 4%.

One outstanding issue is that in case of non-radiating surfaces ($\epsilon = 0$), equation (6.10) exactly coincides with the well-known composite-relation proposed by Bar-Cohen [1] for laminar natural convection in parallel vertical ($cos\theta = 1$) asymmetric isothermal plates. Bar-Cohen's relation was based on the analytical solutions for the two limiting situations of fully developed laminar flow and laminar flow along an isolated plate and was validated with experimental data obtained in short channels.

The main results of the fitting process are shown in Fig. 6.4. The heat transfer relation (6.10) for the Nusselt number is presented in Fig. 6.4a in terms of the parameter $(b/L)Ra_b cos\theta$ (abscissas) and ϵ (five different lines corresponding to the values $\epsilon = 1$, 0.75, 0.5, 0.25 and 0).

The composite-relation of Bar-Cohen for laminar natural convection in parallel

vertical asymmetric plates overlaps the curve for $\epsilon = 0$. On the other hand, the composite-relation for symmetric isothermal plates (both plates isothermal), also given by Bar-Cohen, is presented in Fig. 6.4a with a dashed line. This relation is used here for convenience with the Nusselt number as defined in equation (6.1), even though this is not the standard definition for symmetric isothermal plates, see [1].

The limiting situation of fully developed laminar flow (fully developed limit) and laminar flow along an isolated plate (isolated plate limit) are indicated in the figure by an arrow. While Nu_b in the fully developed limit for symmetric or asymmetric isothermal plates is identical, in the isolated plate limit Nu_b of the symmetric isothermal plates is twice as large than that of the asymmetric isothermal plates.

For $(b/L)Ra_b cos\theta$ values larger than 10^2, the physical phenomena tends towards the isolated plate limit. For these cases and at a fixed value of $(b/L)Ra_b cos\theta$, Nu_b increases with the ϵ from the value corresponding to asymmetric plates to the value corresponding to symmetric plates. However, the Nu_b of the symmetric plates situation is never reached. This is explained by the fact that the lower plate is unable to reach the temperature of the isothermal plate along the entire channel even in situations using black surfaces ($\epsilon = 1$).

In the situations studied here $(b/L)Ra_b cos\theta$ is never below around $5 \cdot 10^0$. In spite of that, the heat transfer relation (6.10) is also consistent in this zone with the results of Bar-Cohen (fully developed limit). All the computed Nu_b presented here tend to converge to the fully developed limit solution for low values of $(b/L)Ra_b cos\theta$, showing no dependency of the plate emissivity.

The relative errors between the fitted data and the heat transfer relation (6.10) are pictured in Fig. 6.4b in terms of $(b/L)Ra_b cos\theta$. Major deviations are observed for $(b/L)Ra_b cos\theta$ values between $5 \cdot 10^0$ and 10^2. According to Bar-Cohen [1], equation (6.10) is a composite relation derived from a linear superposition of two known limiting expressions within which the Nu_b varies smoothly (i.e. the fully developed limit and the isolated plate limit). The zone with major observed relative errors coincides with the intermediate zone between the two limiting expressions, were such kind of composite relation has more problems to properly accommodate the data. As observed, equation (6.10) fits pretty accurately all data (with a maximum relative error below 8%) if $(b/L)Ra_b cos\theta$ is larger than 10^2.

Fitting errors in the intermediate zone could be reduced by a fitting procedure permitting the variation of the constant that affects the first term of equation (6.10) together with the two exponents affecting ϵ. The following relation has been obtained:

$$Nu_b = \left[\left(\frac{2}{29}(b/L)Ra_b cos\theta \right)^{-2} + \left(0.59[(b/L)Ra_b cos\theta]^{1/4}[1 + \epsilon^{4/5}]^{4/5} \right)^{-2} \right]^{-1/2} \quad (6.11)$$

$(b/L)Ra_b cos\theta$	ϵ	Nu_b		
		experimental	*numerical*	*fit (equation 6.10)*
$3.2 \cdot 10^2$	1	4.18 (2.6 %)	4.31 (0.5 %)	4.29
$5.1 \cdot 10^2$	1	5.01 (3.3 %)	4.98 (2.7 %)	4.85
$6.7 \cdot 10^2$	1	5.52 (6.1 %)	5.40 (3.8 %)	5.20
$8.7 \cdot 10^2$	1	6.09 (9.5 %)	5.86 (5.4 %)	5.56

Table 6.3: Comparison of the Nu_b obtained from the experiment, from the numerical model and from the heat transfer relation 6.10. Relative differences respect to the value corresponding to the heat transfer relation are indicated within brackets in %.

The maximum relative fitting errors of this relation are below 9% and the average relative errors around 2%. However, this relation is not consistent with the solution of the fully developed limit for low values of $(b/L)Ra_b cos\theta$, as the fitted parameter 2/29 has been applied instead of 1/12 (that arises from the analytical solution of the fully developed limit).

6.6.3 Validation

As a final step to asses the credibility of the heat transfer relation, the results of a validation test are presented in this section. The direct comparison of solutions of the numerical model to the experimental heat transfer and fluid flow data obtained (see section 6.5) are discussed. Numerical solutions used in this validation test have been carried out reproducing the experimental conditions.

The numerical and experimental values of the Nusselt numbers are given in Table 6.3 together with the corresponding values from the heat transfer relation (6.10). Relative differences to the Nu_b from the heat transfer relation are also indicated and have always kept below 10%.

The comparison of the numerical and experimental fluid flow data is shown in Fig. 6.5 and Fig. 6.6. They respectively correspond to the case of $T_w = 70^oC$ and $T_w = 150^oC$. Compared is the u component of the velocity normalized by the reference velocity $v_{ref} = [Lg\beta(T_w - T_a)cos\theta]^{1/2}$. The upper index * indicates that u has been normalized. Both figures are made up by two sets of data. At the bottom there are the velocity profiles at the central vertical section of each observation window. At the top there are the maps of local differences $\Delta u^*(x,y)$ between the numerical and experimental data in the four observation windows. These maps of differences have been obtained by interpolating the experimental and numerical data at the nodes of a regular mesh of $50 * 50$ nodes, and by calculating the differences
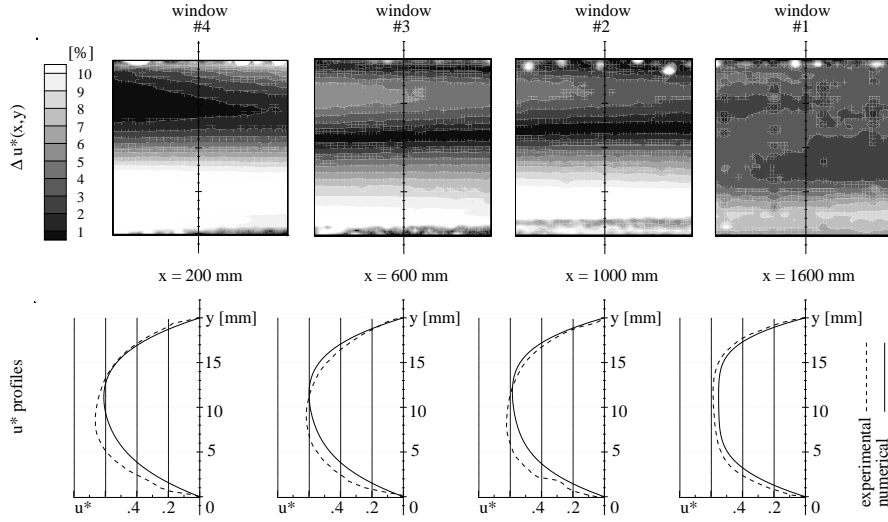
Figure 6.5: Comparison of the u-velocity obtained from the experimental set-up and from the numerical model for $T_w = 70^oC$ and $T_a =laboratory\ temperature$. Top: map of differences in the four observation windows. Bottom: profiles at the central vertical section of each observation window. (Note: * means the u-velocity is normalized by the reference velocity $v_{ref} = [Lg\beta(T_w - T_a)cos\theta]^{1/2}$).

at each one of the nodes. Third order accurate interpolations have been used so as not to introduce additional errors in the data-processing. Apart from a few local large differences in some nodes arisen from errors in the experimental data (white gaps close to the top walls), all local differences in the u^* are below 10%. However, the experimental u^*-profiles are not perfectly reproduced by the numerical profiles. Experimental measurements at the window # 2 of the case with $T_w = 70^oC$ and at the windows # 2 and # 3 for $T_w = 150^o$ show an irregular velocity profile close to the bottom wall. There is no clear explanation of these irregularities in the u-profile and, therefore would require further investigation.

6.7 Conclusions

A parametric numerical study has been performed to obtain a relation of the Nusselt number for free air ($Pr = 0.71$) convection in asymmetric radiative coupled isothermal large plates. Variations in the channel length, the inter-plate spacing, the incli-
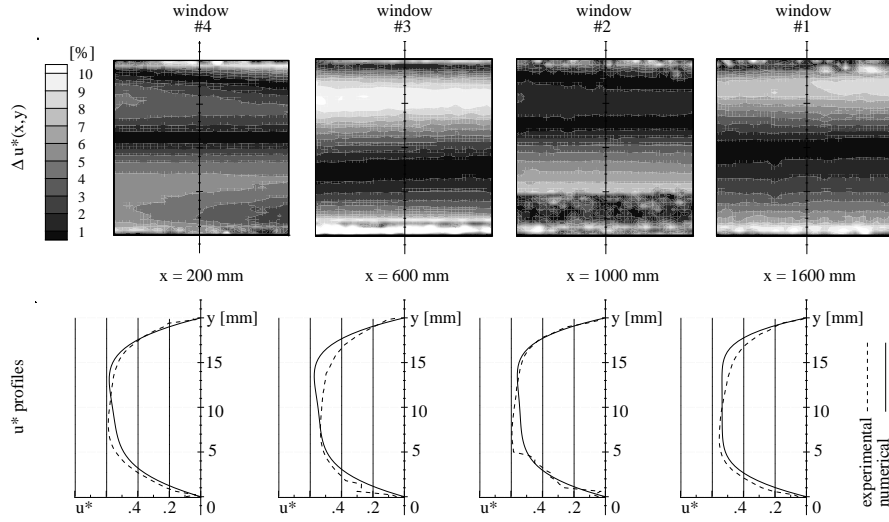
Figure 6.6: Comparison of the *u*-velocity obtained from the experimental set-up and from the numerical model for $T_w = 150^oC$ and $T_a = laboratory$ *temperature*. Top: map of differences in the four observation windows. Bottom: profiles at the central vertical section of each observation window. (Note: * means the the *u*-velocity is normalized by the reference velocity $v_{ref} = [Lg\beta(T_w - T_a)cos\theta]^{1/2}$).

nation of the channel, the plates emissivity and the temperature difference between the isothermal wall and the ambient have been taken into account. The channels under study were out of the applicability range of the heat transfer relations already presented by other authors, and that seemingly were limited to small aspect ratios, lower Grashof numbers and did not consider radiation heat transfer.

The parametric study has consisted in 2500 different cases. All numerical solutions have been submitted to a verification process obtaining estimates for their numerical uncertainty and order of accuracy, and assessing their credibility.

The Nusselt number of all those credible solutions have been fitted to a relation in terms of two numbers: the surface emissivity and a modified Rayleigh number including the channel aspect ratio and the inclination angle. In the case of non-radiating vertical plates, the equation coincides with the previously available composite-relations for lower Grashof numbers.

A final validation test has been carried out by comparing numerical data with

experimental heat transfer and fluid flow data measured in a ad-hoc experimental set-up. The fluid flow has been measured by a Digital Particle Image Velocimetry device.

6.8 Acknowledgments

References

[1] A. Bar-Cohen and W.M. Rohsenow. Thermally optimum spacing of vertical, natural convection cooled, parallel plates. *Journal of Heat Transfer*, 106:116–123, 1984.

[2] E.M. Sparrow, G.M. Chrysler, and L.F. Azevedo. Observed flow reversals and measured-predicted nusselt numbers for natural convections in a one-sided heated vertical channel. *Journal of Heat Transfer*, 106:325–332, 1984.

[3] L.F.A. Azevedo and E.M. Sparrow. Natural convection in open-ended inclined channels. *Journal of Heat Transfer*, 107:893–901, 1985.

[4] J. Cadafalch, C.D. Pérez-Segarra, R. Cònsul, and A. Oliva. Verification of finite volume computations on steady state fluid flow and heat transfer. *Journal of Fluids Engineering*, 124:11–21, 2002.

[5] P.J. Roache. Perspective: a method for uniform reporting of grid refinement studies. *Journal of Fluids Engineering*, 116:405–413, 1994.

[6] C.D. Pérez-Segarra, A. Oliva, M. Costa, and F. Escanes. Numerical experiments in turbulent natural and mixed convection in internal flows. *International Journal for Numerical Methods for Heat and Fluid Flow*, 5(1):13–33, 1995.

[7] P.H. Gaskell et al. Comparison of two solution strategies for use with higher-order discretization schemes in fluid flow simulation. *International Journal for Numerical Methods in Fluids*, 8:1203–1215, 1988.

[8] S.R. Marthur and J.Y. Murthy. Pressure boundary conditions for incompressible flow using unstructured meshes. *Numerical Heat Transfer, Part B*, 32:283–298, 1997.

[9] S.V. Patankar. *Numerical heat transfer and fluid flow*. Hemiosphere Publishing Corporation, 1980.

[10] J.P. Van Doormal and G.D. Raithby. Enhancements of the simple method for predicting incompressible fluid flows. *Numerical Heat Transfer*, 7:147–163, 1984.

[11] Westerweel J. Efficient detection of spurious vectors in particle image velocimetry. *Experiments in Fluids*, 16:236–247, 1994.